INORGANIC CHEMISTRY FRONTIERS

RESEARCH ARTICLE

View Article Online
View Journal | View Issue

Cite this: *Inorg. Chem. Front.*, 2023, **10**, 4471

Fabrication of heterostructured Pd-porphyrin MOFs/$ZnIn_2S_4$ composites to boost photocatalytic hydrogen evolution under visible light irradiation†

Sheng Wang,[a] Huiyi Feng,[a] Chenglong Zheng,[a] Shihao Li,[a] Shilu Fan *[a] and Yi-Si Feng *[a,b]

The purposeful and sensible fabrication of novel binary-shelled photocatalysts is highly attractive for photocatalytic hydrogen evolution. In this work, $ZnIn_2S_4$ (ZIS) nanosheets were induced to grow on a framework of Pd-porphyrin MOFs (Pd-PMOFs) to construct novel binary-shelled nanotubes (Pd-PMOFs@ZIS) *via* a multistep solvothermal process. On account of the abundant active sites, well-matched band gaps, strong visible light harvesting capability and outstanding charge migration efficiency, the assembled Pd-PMOFs@ZIS heterostructures exhibited prominently enhanced photocatalytic hydrogen generation activity. Concretely, the hydrogen evolution rate of the optimized sample was up to 8200.25 μmol g^{-1} h^{-1} under visible light irradiation, which was approximately 24.07 and 13.73 times larger than those of individual ZIS and Pd-PMOFs, respectively. More importantly, density functional theory (DFT) calculations demonstrated that the fabrication of the heterojunctions established electron transport channels with Pd and In ions showing strong covalent bonding, and the electrons were converged and consumed at the interfaces between Pd-PMOFs and ZIS. Specifically, the transfer pathway of electrons is from Pd-PMOFs to ZIS. Our work provides a convenient and advanced prototype for synthesizing binary heterojunction photocatalysts with superior charge separation and transfer efficiency.

Received 1st May 2023,
Accepted 28th June 2023

DOI: 10.1039/d3qi00803g

rsc.li/frontiers-inorganic

1. Introduction

Porphyrins are highly conjugated π-electron heterocyclic macromolecules, such as cytochromes and chlorophylls, widely found in natural animals and plants.[1,2] By virtue of larger specific surface areas, abundant pore channels, wide visible light absorption, and flexible structures, porphyrins have been applied in various fields, covering biomimetic chemistry, catalysis, and biological detection.[3–5] Porphyrins as functional molecules are usually used in homogeneous systems, which goes against sustainable recycling. Therefore, great efforts have been devoted to the development and design of porphyrin based complexes for applications in heterogeneous systems in the past few decades.[6–9] Among them, porphyrin based metal organic frameworks (PMOFs) have received substantial attention.[10–12] As an important subclass of MOFs, PMOFs are novel porous crystalline materials arranged in a periodic pattern and composed of porphyrin molecules as structural units and metal ions or metal clusters.[13,14] Due to the large number of active sites between metal clusters and organic ligands, many new multifunctional porphyrin compounds can be synthesized by tuning the metal centers, organic ligands, and reaction conditions.[15,16] Such abundant and adjustable structures play an active role in expanding the application of PMOF materials, especially in photocatalysis.[17,18] At present, the research efforts in photocatalysis are primarily focused on the selective conversion of various organics, the degradation of pollutants in water, and oxygen or hydrogen production from water splitting.[19–21] It is worth emphasizing that in response to the energy crisis, a wide variety of photocatalysts have been developed for efficient photocatalytic hydrogen production, including TiO_2,[22] g-C_3N_4,[23] Zr-MOFs,[24] and $ZnIn_2S_4$.[25] Among them, $ZnIn_2S_4$ (ZIS) as a ternary sulfide with a layered structure and stable chemical properties is a promising visible-light responsive photocatalyst.[26] However, the photocatalytic activity of single-component catalysts is still impeded or restricted by the rapid recombination of photo-induced electrons and holes. Therefore, it is of great significance to develop photocatalysts with multicomponent composites for the enhancement of the mobility of carriers. For instance, Zhang *et al.* reported that

[a]*School of Chemistry and Chemical Engineering, Hefei University of Technology, Hefei 230009, Anhui, China. E-mail: fengyisi@hfut.edu.cn, fanshilu@hotmail.com*
[b]*Anhui Province Key Laboratory of Advance Catalytic Materials and Reaction Engineering, Hefei 230009, P. R. China*

† Electronic supplementary information (ESI) available. See DOI: https://doi.org/10.1039/d3qi00803g

MoS_2 quantum dots/$ZnIn_2S_4$ photocatalysts with a two-dimensional (2D) atomic-level heterostructure exhibited improved electron transfer capability.[27] Wang *et al.* synthesized $ZnIn_2S_4$/In_2O_3 hierarchical tubular heterostructures. This design accelerates the separation and transfer of photogenerated charges, and exposes abundant active sites for surface catalysis.[28] Some researchers have also developed the combination of $ZnIn_2S_4$ and metal organic framework (MOF) materials. Jin *et al.* fabricated PCN-224@$ZnIn_2S_4$ composites with a novel hierarchical structure *via* a facile solvothermal method.[29] The optimized $ZnIn_2S_4$@PCN-224 displayed a hydrogen production rate of 0.284 mmol h^{-1}. Liu *et al.* developed a series of heterostructured $ZnIn_2S_4$@NH_2-MIL-125(Ti) nanocomposites with different NH_2-MIL-125(Ti) contents as carriers.[30] The results manifested that the optimal content of NH_2-MIL-125(Ti) was about 40 wt% and its photocatalytic hydrogen evolution rate was 2204.2 μmol h^{-1} g^{-1}, which was 6.5 times higher than that of pure $ZnIn_2S_4$. Therefore, the construction of $ZnIn_2S_4$ based composites can produce a lot of unique high-speed charge transfer nanochannels at heterogeneous interfaces, thus contributing to the transfer efficiency of electron hole pairs and achieving outstanding photocatalytic activity.[31] However, thus far, no report is available on the construction of Pd-porphyrin MOFs@$ZnIn_2S_4$ nanosheet photocatalysts.

In this present work, a series of hierarchical Pd-porphyrin MOFs@$ZnIn_2S_4$ (Pd-PMOFs@ZIS) composites were firstly designed and fabricated through *in situ* growth of unique ZIS nanosheets on the surface of rod-like Pd-porphyrin MOFs *via* a simple one-step solvothermal method. Usually, *in situ* encapsulation is favorable for the formation of contact interfaces and the enhancement of stability for the prepared composite materials.[32] The resultant Pd-PMOFs@ZIS photocatalyst exhibited a significant hydrogen generating activity in comparison with pure $ZnIn_2S_4$ nanosheets under simulated sunlight irradiation. This work aims to suggest that the increased electron–hole separation efficiency and improved visible-light absorption for the Pd-PMOFs@ZIS photocatalyst can facilitate photocatalytic splitting of water.

2. Experimental section

2.1. Materials

Zinc chloride ($ZnCl_2$, 99%), indium chloride ($InCl_3{\cdot}xH_2O$, 99%), thioacetamide (C_2H_5NS, 99%), *N*,*N*-dimethylacrylamide (DMF, 99%) palladium nitrate and ($Pd(NO_3)_2$, 97%) were purchased from Sinopharm Chemical Reagent Co., Ltd. All chemicals were used without further purification unless otherwise stated.

2.2. Synthesis of Pd modified porphyrin MOFs (Pd-PMOFs)

The tetrakis(4-carboxyphenyl)porphyrin (TCPP) was prepared according to previous work. The Pd modified porphyrin MOFs (Pd-PMOFs) were synthesized according to a solvothermal method. Typically, 15 mg of $Pd(NO_2)_2{\cdot}2H_2O$, 35 mg of TCPP, and 20 mL of DMF were all added into a 30 mL beaker. The homogeneous mixed solution was formed by sonication. The mixture was then transferred to a 50 mL Teflon-lined autoclave and incubated at 120 °C for 4 h. After cooling down to room temperature, the single crystal materials of Pd-PMOFs were collected by natural sedimentation and washed with acetone and ethanol several times.

2.3. Synthesis of Pd-PMOFs@$ZnIn_2S_4$ composites

The encapsulation of $ZnIn_2S_4$ nanosheets on the surface of the Pd-PMOFs was achieved by a one-step solvothermal method. In an optimized preparation procedure, 0.33 g of $ZnCl_2$, 1.11 g of $InCl_3{\cdot}xH_2O$, 2.50 g of C_2H_5NS and 0.1 g Pd-PMOFs were dispersed into 50 mL of deionized water and stirred for 20 min. Then, the entire solution was transferred into a 100 mL autoclave and kept at 160 °C for 5 h. Finally, the powder was obtained by filtration and washed several times with deionized water, and then dried at 60 °C. By controlling the mass ratio of Pd-PMOFs to $ZnIn_2S_4$ (1 : 15, 1 : 10 and 1 : 5), a series of composites were prepared and labeled as Pd-PMOFs/ZIS-1, Pd-PMOFs/ZIS-2 and Pd-PMOFs/ZIS-3. Furthermore, to form a contrast, pure $ZnIn_2S_4$ was synthesized through the above steps without Pd-PMOFs. The detailed synthetic pathway is shown in Fig. 1.

2.4. Characterization

The actual crystal phases of powders were characterized on X-ray diffractometry (PANalytical, Netherlands). The microstructure and elemental distribution of the samples were observed using an SU8020 Scanning Electron Microscope (SEM, Hitachi, Japan) and a transmission electron microscope (TEM, JEM1400FLASH). The fluorescence emission spectral data were collected using HITACHI F7000. The elemental species of the samples were detected by using X-ray Photoelectron Spectroscopy (XPS, Thermo, USA). The photocurrent and impedance data of the samples were obtained on an electrochemical workstation (KM1-CS1006) with a glassy carbon electrode as the working electrode and a calomel electrode as the reference electrode. The UV-vis spectroscopy data of the solid powders were acquired from the UV-Vis spectrophotometer (Agilent UV-2450). The actual Pd content in Pd-PMOFs@ZIS-2 evaluated by inductively coupled plasma atomic emission spectroscopy (ICP-AES) analysis.

2.5. Photocatalytic hydrogen evolution experiments

Photocatalytic H_2 evolution experiments were accomplished in a Perfectlight labsolar 6A photoreactor. A 300 W Xe lamp was used as simulated solar light ($\lambda \geqq 420$ nm). The corresponding focusing intensity is 180 mW cm^{-2}. Typically, 50 mg of sample was added into 100 mL of aqueous solution containing 10 mL of triethanolamine. The generated hydrogen gas was detected using a gas chromatograph (GC9790II-PLF-01) with a TCD detector and argon as the carrier gas.

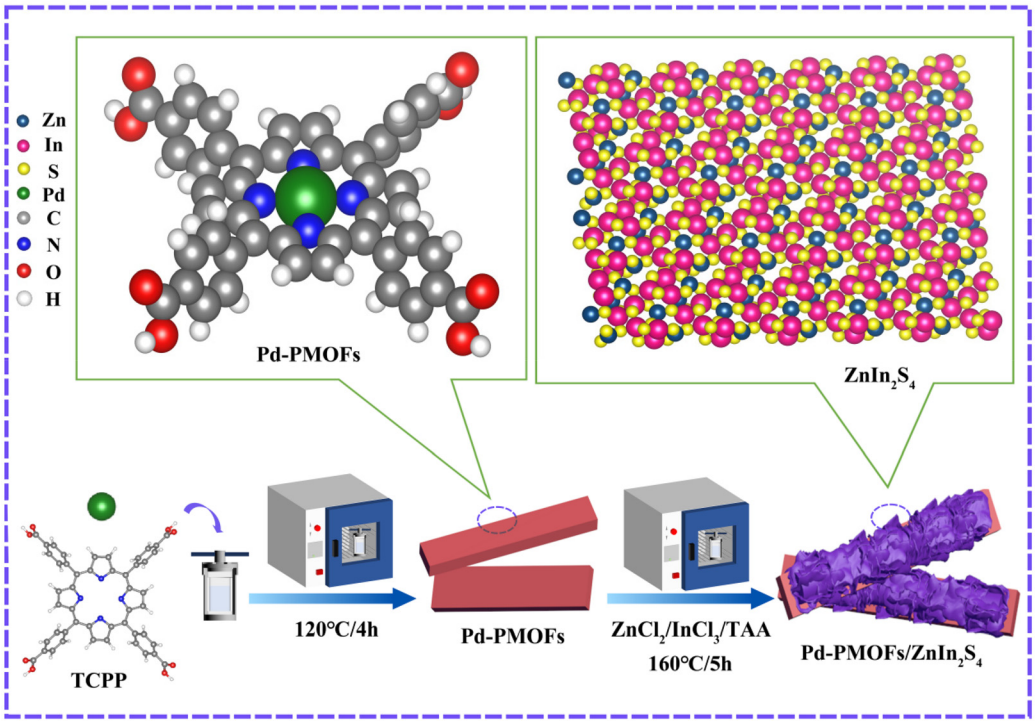

Fig. 1 Schematic representation of the synthetic procedure of Pd-PMOFs/ZIIn$_2$S$_4$ composites.

3. Results and discussion

X-ray diffraction analysis (XRD) was performed to explore the crystallization status of the prepared pure ZIS, Pd-PMOFs and Pd-PMOFs@ZIS composites. As exhibited in Fig. 1a, the pure ZIS presented visible characteristic peaks at 2θ = 21.2°, 27.7°, and 47.3°, which were assigned to (006), (102) and (110) lattice planes for ZIS with a hexagonal phase, respectively (JCPDS No. 65-2023).[33] There are five main diffraction peaks at about 2θ = 6.3°, 10.1°, 10.9°, 17.7° and 21.0° for pristine Pd-PMOFs. When sufficient ZIS nanosheets were loaded onto the surface of the Pd-PMOFs, it was clearly observed that the characteristic diffraction peaks of both Pd-PMOFs and ZIS appeared at the Pd-PMOFs@ZIS-1 sample, declaring the successful construction of such composites. Additionally, the intensity of the peak located at 21.0° increased with the increasing content of Pd-PMOFs in the Pd-PMOFs@ZIS-2 sample, confirming that this peak corresponds to Pd-PMOFs. In particular, the Pd-PMOFs@ZIS-3 composites displayed the apparent diffraction peaks of Pd-PMOFs, which was probably due to the relatively low loading of ZIS.

XPS spectra were used to identify the elemental composition and chemical states of the prepared pure ZIS, Pd-PMOFs and Pd-PMOFs@ZIS composites. As shown in Fig. 2b, the characteristic peaks of zinc, indium, and sulfur elements are easily observed in the pure ZIS sample.[34] Meanwhile, the Pd-PMOFs possessed the main characteristic peaks of carbon, nitrogen, oxygen and palladium. Significantly, the Pd-PMOFs@ZIS photocatalysts displayed all the characteristic peaks of pure ZIS and Pd-PMOFs, covering C 1s, O 1s, N 1s, Pd 3d, S 2p, In 3d and Zn 2p. As presented in Fig. 2c, the peaks located at 288.5 eV and 284.8 eV are allocated to the O–C=O and C–C groups of C 1s from Pd-PMOFs and Pd-PMOFs@ZIS composites. The N 1s spectrum in pure TCPP exhibits two peaks at 397.2 and 399.5 eV, which are assigned to C=N–C and C–NH–C bonds, respectively.[35] Since Pd^{2+} coordinates with four N atoms on the porphyrin ring, only one peak at 398.2 eV can be intuitively identified in the Pd-PMOF sample, as illustrated in Fig. S1.† For Pd-PMOFs@ZIS composites, in addition to the observed N–Pd peak at 398.5 eV, there are obviously two peaks at 400.0 eV and 401.4 eV, which may be assigned to the C–NH_2 peak of free TAA (Fig. 2d). Furthermore, the C–OH bonds of O1s from Pd-PMOFs@ZIS composites evidently disappeared compared to those of the Pd-PMOFs (Fig. 2e), which may be attributed to the high affinity between the active groups –OH and metal ions, thus inducing the deposition of ZIS on the surface of Pd-PMOFS. Meanwhile, with the content of pristine Pd-PMOFs increasing, the binding energies of C=O for these composites shifted to a higher position toward 531.83, 531.75 and 531.56 eV, respectively, demonstrating a close interfacial connection between Pd-PMOFs and ZIS.[36] From the high-resolution spectrum illustrated in Fig. 2 (g–i), the specific XPS peaks located at 161.49 eV (S $2p_{3/2}$) and 162.63 eV (S $2p_{1/2}$) for S^{2-}, 444.74 eV (In $3d_{5/2}$) and 452.29 eV (In $3d_{3/2}$) for In^{3+}, and 1021.74 eV (Zn $2p_{3/2}$) and 1044.88 eV (Zn $2p_{1/2}$) for Zn^{2+} can be visually distinguished in pure $ZnIn_2S_4$.[37] Meanwhile, the characteristic peaks located at 337.70 eV (Pd $3d_{5/2}$) and 342.91 eV (Pd$3d_{3/2}$) for Pd^{2+} are also

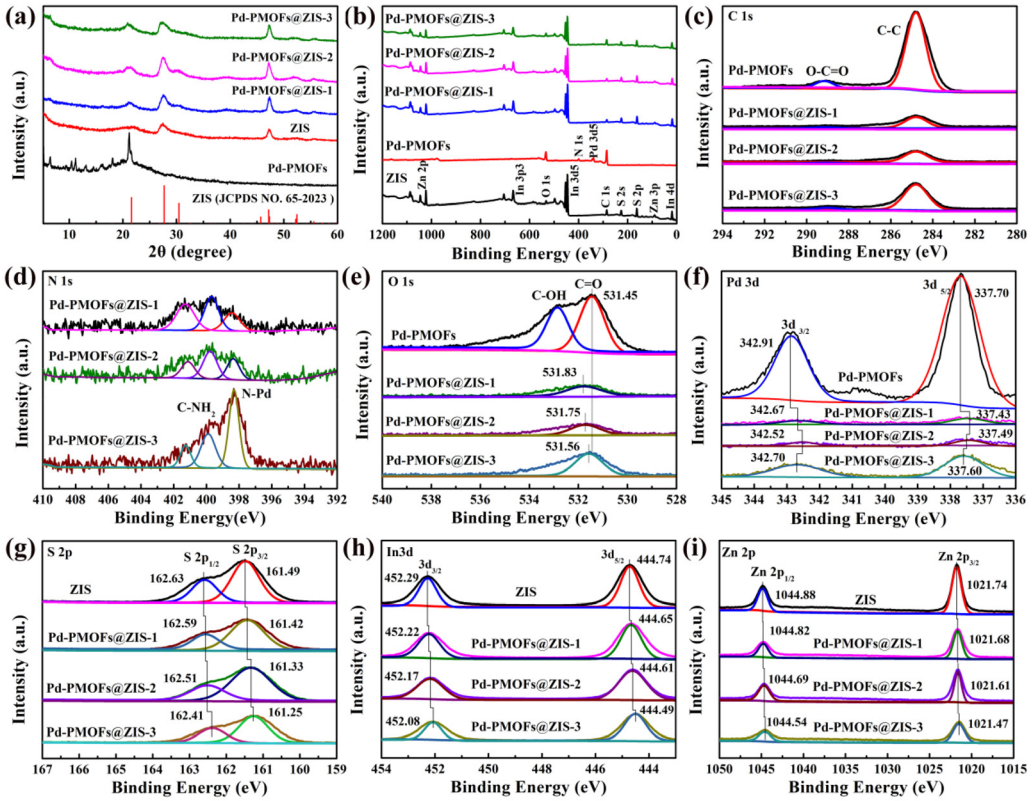

Fig. 2 (a) XRD patterns of the prepared ZnIS, Pd-PMOFs and Pd-PMOFs@ZIS composites. (b) XPS survey spectra for all samples, containing (c) C 1s, (d) N 1s, (e) O 1s, (f) Pd 3d, (g) S 2p, (h) In 3d and (i) Zn 2p.

clearly observed in pure Pd-PMOFs (Fig. 2f). Compared to those in pure ZIS and Pd-PMOFs, such peaks for Pd-PMOFs@ZIS composites shift to the lower binding energy region, indicating that the electrons are transferred from Pd-PMOFs to ZIS and enriched around their interface.[38] This also demonstrates that the formation of heterostructures can modulate the intrinsic electronic structures of pure Pd-PMOFs and ZIS.[39]

The detailed morphologies and microstructures of the resultant pure ZIS, Pd-PMOFs and Pd-PMOFs@ZIS composites were examined using SEM and TEM images. As seen in Fig. 3 (a and f), the pure ZIS displayed a flower-like aggregated morphology consisting of uniform nanosheets. The prepared Pd-PMOFs showed a regular rectangular structure with an approximate length of 12 μm and a width of about 4 μm (Fig. 3b). Compared with pure ZIS and Pd-PMOFs, the fabricated Pd-PMOFs@ZIS composites demonstrated a distinct hierarchical structure. Specifically, when loaded with excessive ZIS, as presented in Fig. 3c, it can be clearly observed that the abundant flower-like microspheres formed by the aggregation of ZIS nanosheets were closely wrapped around the Pd-PMOF surface in the Pd-PMOFs@ZIS-1 sample, evidencing that the *in situ* growth not only preserved the morphology of ZIS nanosheets, but also contributed to the formation of compact heterostructures.[32,40] With the increase of the carrier content, the aggregated flower-like microsphere morphology of ZIS basically disappeared and 2D ZIS nanosheets were homogeneously coated on the surface of Pd-PMOFs for the Pd-PMOFs@ZIS-2 heterostructure, as shown in Fig. 3d. Such a two-dimensional lamellar structure for ZIS was also more evident in the Pd-PMOFs@ZIS-3 sample (Fig. 3e). Meanwhile, these TEM images visually demonstrated how the nanosheets of ZIS were tightly attached to the surface of Pd-PMOFs, as pronounced in Fig. 3(f–h). It is noteworthy that this core–shell structure became progressively lighter in color and thinner in thickness as the content of the carrier increased, which is basically consistent with the above SEM results. In addition, the interplanar distance of the lattice fringes for the ZIS nanosheets anchored on the shell layer of Pd-PMOFs was measured by high-resolution TEM (HRTEM) to be about 0.32 nm, corresponding to the (102) crystal plane of the hexagonal structure.[41] Energy dispersive X-ray spectroscopy (EDS) was employed to determine the corresponding elemental composition in the Pd-PMOFs@ZIS-3 photocatalyst. From the mapping images in Fig. 3(k–s), it can be visualized that the elements containing C, N, O, Pd, S, In and Zn are portrayed in their distinctive colors. All the discerned elements were evenly distributed over the fixed region, exhibiting that the ZIS nanosheets were uniformly located on the skeleton of Pd-PMOFs. Consequently, the observations from the analyses including XRD, XPS, EDS and HRTEM all validated the successful construction of Pd-PMOFs@ZIS heterostructures.

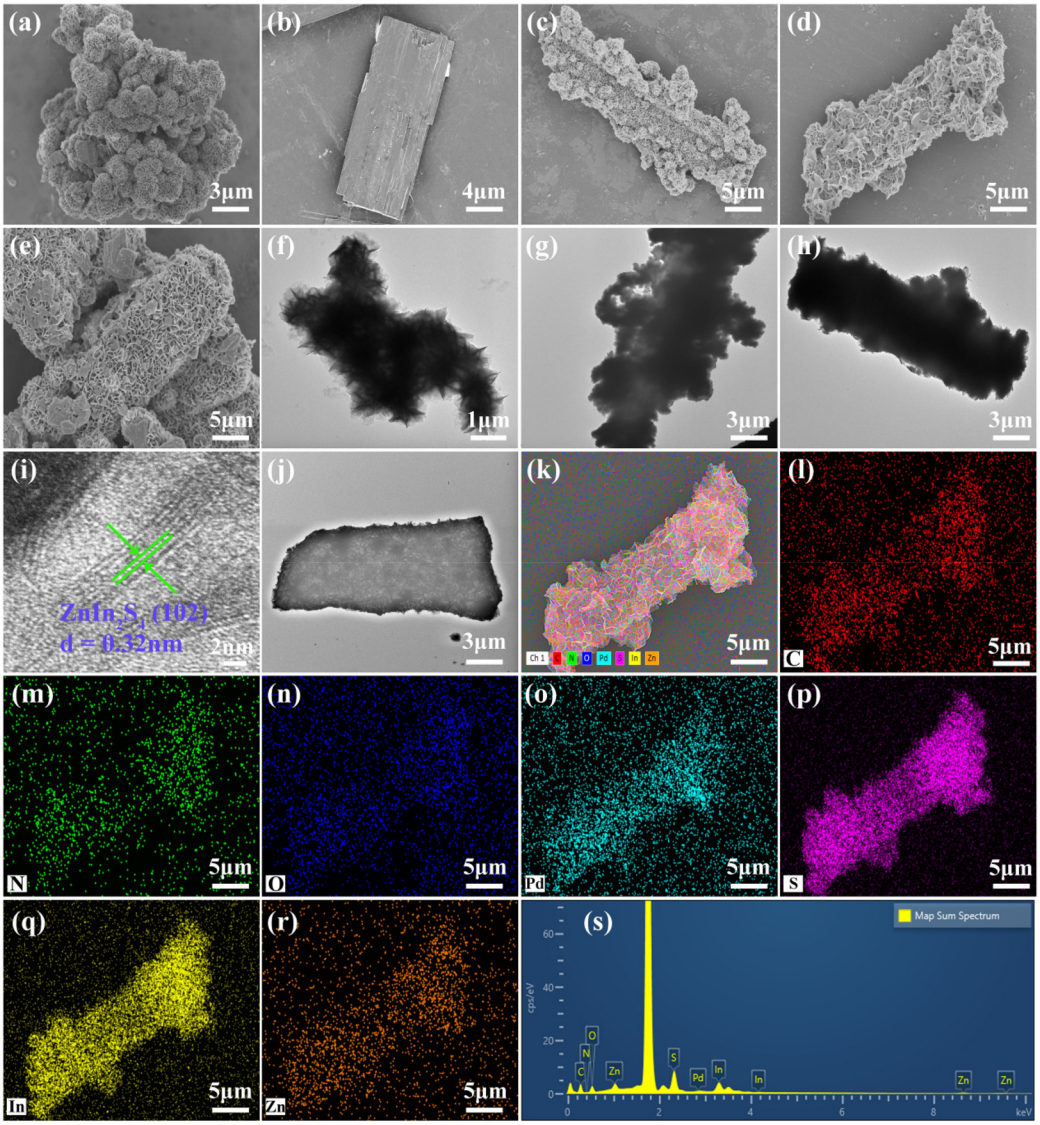

Fig. 3 FESEM and TEM images of samples: (a and f) ZIS, (b) Pd-PMOFs, (c and g) Pd-PMOFs@ZIS-1, (d, h and i) Pd-PMOFs@ZIS-2, and (e and j) Pd-PMOFs@ZIS-3. (k–r) Elemental mappings and (s) EDX spectrum of Pd-PMOFs@ZIS-2.

Fig. 4a shows the UV-Vis diffuse reflectance spectra (DRS) of the as-fabricated photocatalysts. As observed, the pure ZIS solid powder had a broad absorption edge at around 530 nm, while Pd-PMOFs possessed a light absorption edge at about 650 nm. After loading Pd-PMOFs, the absorption edge of Pd-PMOFs@ZIS composites exhibited a significant red shift in comparison with pure ZIS. In particular, the light absorption intensity of this Pd-PMOFs@ZIS-2 sample was also substantially higher than that of the single-component photocatalyst in the region of 420–800 nm, indicating that the combination of ZIS and Pd-PMOFs optimized the band gap and visible light absorption capacity, which was beneficial for further promotion of the photocatalytic hydrogen production activity.[42] According to Kubelka–Munk function and the Tauc plot,[43] the band gap energies (E_g) of selected pure ZIS, Pd-PMOFs and Pd-PMOFs@ZIS-2 samples were calculated to be 2.14, 1.72 and 1.68 eV, respectively. Moreover, the flat-band potential (E_{FB}) values of the representative photocatalysts were estimated using the Mott–Schottky plots. As presented in Fig. 4(d–f), the ZIS, Pd-PMOFs and Pd-PMOFs@ZIS composites all demonstrated typical n-type semiconductor properties due to their inherent positive slope.[44] Based on the equation for the standard hydrogen electrode with (E(NHE) = E(Ag/AgCl) + 0.197), the E_{FB} values of ZIS, Pd-PMOFs and Pd-PMOFs@ZIS-2 can be identified as −0.923, −1.013 and −0.623 V *vs.* NHE. For such an n-type semiconductor, its flat-band potential is typically 0.1–0.3 eV higher than the conduction band (CB) potential.[45] Accordingly, the E_{FB} values of the selected photocatalysts are approximately equal to their conduction band (CB) values.[46] As a result, the conduction band (CB) values of ZIS, Pd-PMOFs and Pd-PMOFs@-2 samples were derived as −1.12 eV, −1.21 eV and −0.68 eV, respectively. Furthermore, Fig. 4(g and h) show

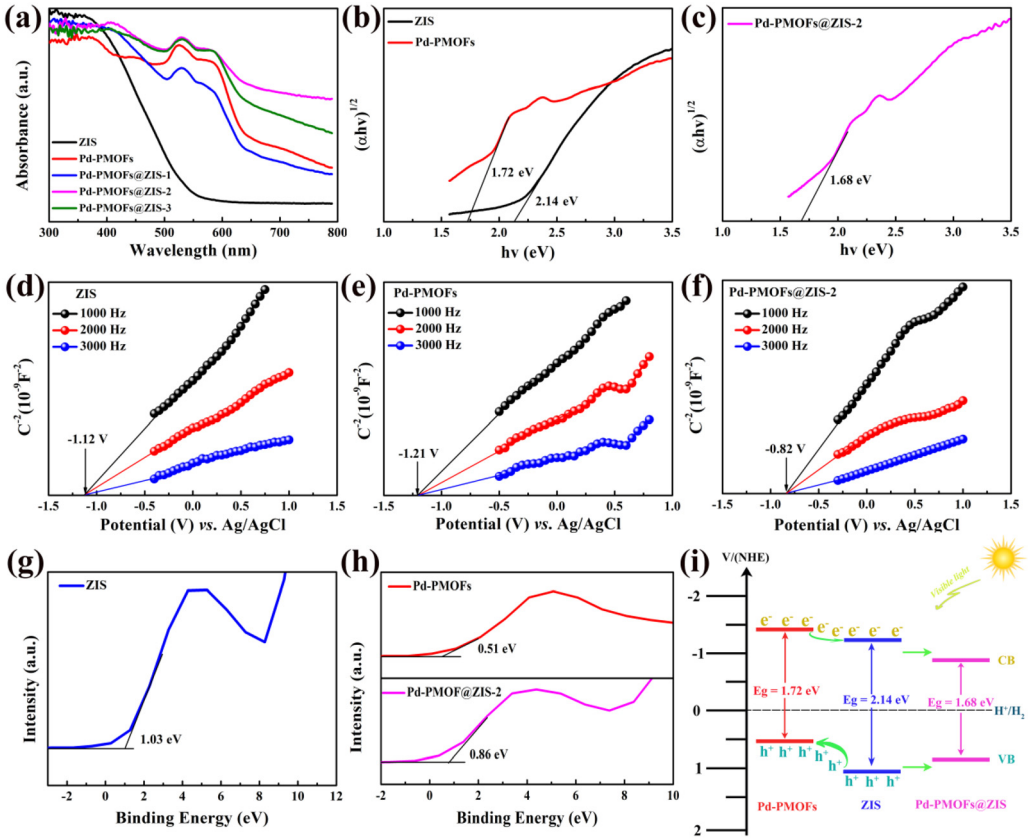

Fig. 4 (a) UV-vis DRS and (b and c) plots of $(\alpha h\nu)^{1/2}$ *versus* $(h\nu)$ for the bandgap energy of the synthesized catalysts. (d–f) Mott–Schottky plots collected at various frequencies, (g and h) valence band (VB) XPS spectra and (i) band alignments of the selected samples.

the valence band (VB) position of the corresponding samples determined by XPS spectroscopy. As presented, the valence band (VB) values of ZIS, Pd-PMOFs and Pd-PMOFs@ZIS-2 photocatalysts were 1.03 eV, 0.51 and 0.86 eV, respectively, which highly matched the difference between their band gap energy (E_g) and valence band (VB). The corresponding energy band positions of these selected photocatalysts are displayed in Fig. 4i. According to the well matched energy band structures of ZIS and Pd-PMOFs, the type of Pd-PMOFs@ZIS heterostructure was identified to be a type II interleaved n–n junction.[47,48]

The transient photocurrent responses with the light switch off and on cycles of all photocatalysts were studied under visible light irradiation ($\lambda \geqq 420$ nm), as shown in Fig. 5(a). Notably, the transient photocurrent response density for the Pd-PMOFs@ZIS-2 catalyst was significantly enlarged compared with the pristine Pd-PMOFs and ZIS. Their intensity levels were in the order of Pd-PMOFs@ZIS-2 > Pd-PMOFs@ZIS-3 > Pd-PMOFs@ZIS-1 > Pd-PMOFs or ZIS, illustrating that the binary shell heterostructure between ZIS nanosheets and Pd-PMOF carriers can effectively promote the separation and migration of photoinduced electron–hole pairs.[49] Electrochemical impedance spectroscopy (EIS) was applied to further analyze the transport efficiency of photogenerated charge carrier pairs (Fig. 5b). In general, the smaller the ESI arc radius in the Nyquist plot, the lower the transfer resistance of photoexcited carriers.[50] In comparison with ZIS and Pd-PMOFs, the acquired Pd-PMOFs@ZIS composites exhibited a smaller diameter of the Nyquist semicircle, and the optimal photocatalyst exposed the lowest impedance, which suggested that the interface formed by the heterojunction was favorable for charge transfer. From another perspective, to explore the recombination of photoinduced electron–hole pairs, the steady photoluminescence (PL) spectral data of all catalysts are displayed in Fig. 5c. Bare ZIS manifested the highest PL emission intensity at around 750 nm, mainly due to the maximum recombination rate of charge carriers.[51] Meanwhile, the Pd-PMOFs showed significant Q band absorption peaks from porphyrin in the visible light region.[35] Although the Pd-PMOFs@ZIS composites demonstrated similar PL profiles, their PL emission intensities had sharply decreased in comparison with those of pristine Pd-PMOFs and ZIS, confirming that the fabrication of the binary shell heterojunctions was beneficial for suppressing the recombination of photo-excited electron-holes. In particular, the Pd-PMOFs@ZIS-2 sample exhibited the lowest PL intensity, indicating that the catalyst with the optimal photocatalytic activity could be screened by adjusting the ratio of single-component catalysts. Also, the charge carrier lifetimes for the corresponding catalysts were evaluated using the time-resolved photoluminescence (TRPL)

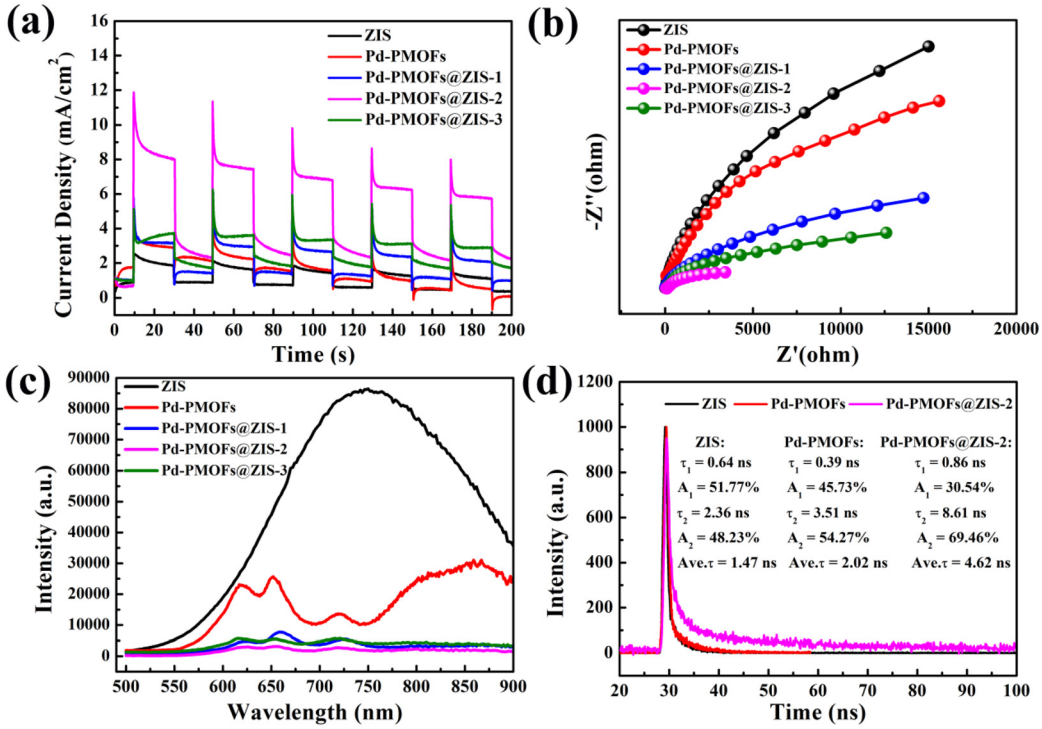

Fig. 5 (a) Transient photocurrent responses of all the catalysts. (b) EIS plots, (c) PL spectra and (d) lifetime decay curves of the selected catalysts.

spectra. As listed in Fig. 5d, owing to the longer average emission lifetime in Pd-PMOFs@ZIS-2 (4.62 ns) than that in ZIS (1.47 ns) and Pd-PMOFs (2.02 ns), the electrons generated from the heterostructure of Pd-PMOFs@ZIS-2 are more easily transferred from the active center of Pd to the ZIS interface and they participate in the reaction, thus enhancing the photocatalytic hydrogen production performance of such composites.

The hydrogen production activity of the prepared photocatalysts was evaluated under 300 W Xe lamp light illumination ($\lambda \geq 420$ nm) without additional cocatalysts by utilizing triethanolamine (TEOA) as the hole scavenger. As presented in Fig. 6a, the amount of hydrogen produced on all photocatalysis depicted a linear increasing trend with time. As observed, the original ZIS and Pd-PMOFs with 4 h of visible light irradiation showed a total amount of photocatalytic hydrogen production of 1362.88 and 2389.20 μmol g^{-1}, respectively. To take it one step further, the hydrogen production rates were relatively low when individual ZIS (340.72 μmol g^{-1} h^{-1}) and Pd-PMOFs (597.30 μmol g^{-1} h^{-1}) were used as photocatalysts (Fig. 6b), indicating that the single-component catalysts were insensitive to hydrogen stimulation under visible light illumination. However, after embedding ZIS nanosheets onto the Pd-PMOFs support, the Pd-PMOFs@ZIS heterojunctions displayed remarkably enhanced hydrogen generation rates. The maximum hydrogen generation efficiency over the Pd-PMOFs@ZIS-2 composite runs up to 8200.25 μmol g^{-1} h^{-1}, which is approximately 24.07 and 13.73 times higher than those of pure ZIS and Pd-PMOFs, respectively. It is concluded that the improvement in the photocatalytic H_2 evolution for Pd-PMOFs@ZIS composites may be due to the preferable assembly of such a heterogeneous structure between ZIS and Pd-PMOFs, boosting the efficient separation and migration of photoexcited electron–hole pairs.[52] To our satisfaction, the constructed Pd-PMOFs@ZIS-2 photocatalyst still persistently showed prominent photocatalytic hydrogen production activity after six cycle experiments (Fig. 6c). Meanwhile, the apparent quantum efficiency (AQE) of Pd-PMOFs@ZIS-2 possessed an AQE value of 13.17% at 420 nm (Fig. 6d). Moreover, its crystalline structure retained the initial state after recycle tests in the XRD patterns, as shown in Fig. 6e. Although the microstructures of the Pd-PMOFs@ZIS-2 composite had been damaged to some extent due to mechanical stirring during multiple cycling experiments, this sample still exhibited the inseparable framework of such a binary core–shell structure (Fig. 6f). The actual Pd content in Pd-PMOFs@ZIS-2 before and after the reaction was evaluated by inductively coupled plasma atomic emission spectroscopy (ICP-AES) analysis (Fig. S3†). Obviously, there was almost no change in Pd content before and after cycling in the composite system. These results verified that the synthesized Pd-PMOFs@ZIS-2 photocatalyst has excellent reproducibility and stability.

To further investigate the charge transfer for the Pd-PMOFs@ZIS heterojunction, spin-polarized density functional theory (DFT) calculations were performed to determine the variation of Bader charges.[53] The specific step for model construction is shown in the ESI.† The calculated LUMO and HOMO energy levels and energy gaps of pure TCPP were

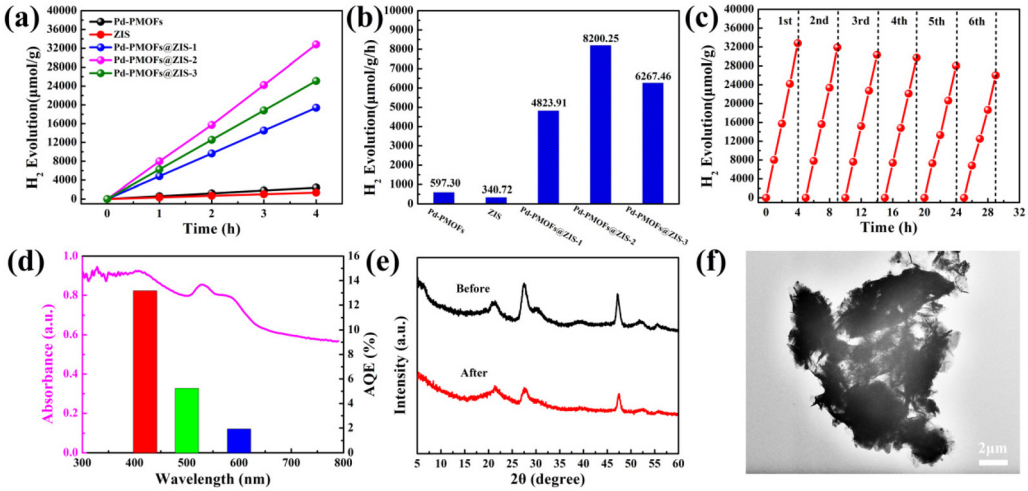

Fig. 6 The hydrogen production amount (a) and rate (b) of the obtained photocatalysts. (c) 6 catalytic cycle tests for the photocatalytic H_2 evolution, and (d) wavelength dependent AQE over the optimized sample. (e) XRD patterns of Pd-PMOFs@ZIS-2 before and after experiments. (f) TEM images of the sample after cycling tests.

−3.01, −5.77 and 2.76 eV, respectively. Meanwhile, the LUMO and HOMO energy levels and energy gaps of Pd-PMOFs are given as −2.72, −4.46 and 1.74 eV, respectively, which basically match the actual test values. The results also further suggested that the introduction of Pd ions into the porphyrin central ring is responsible for changing the intrinsic energy level orbital of TCPP and decreasing its band gap, as shown in Fig. S2.† In addition, the optimized structures of initial Pd-PMOFs and ZIS are visualized in Fig. 7. The Pd-PMOFs were used as carriers to support the (102) crystallographic planes of the ZIS supercell, forming a heterogeneous structure. In Fig. 8a, it can be clearly observed that there is a strong covalent interaction between Pd atoms from Pd-PMOFs and In atoms from ZIS, which can provide convenient charge transfer channels for the Pd-PMOFs@ZIS composites. Fig. 8b suggests the charge density distribution, with the yellow and blue regions representing the accumulation and depletion areas of electron density, respectively. It can be intuitively noted that electrons

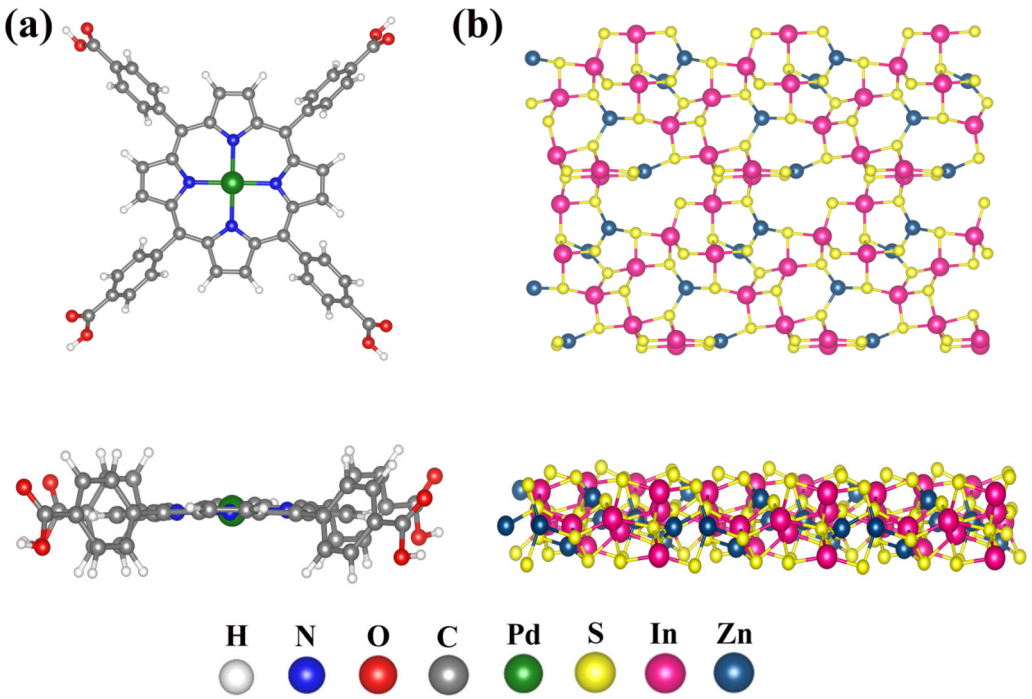

Fig. 7 Top and side views of the Pd-MOFs (a) and $ZnIn_2S_4$ (102) supercell (b).

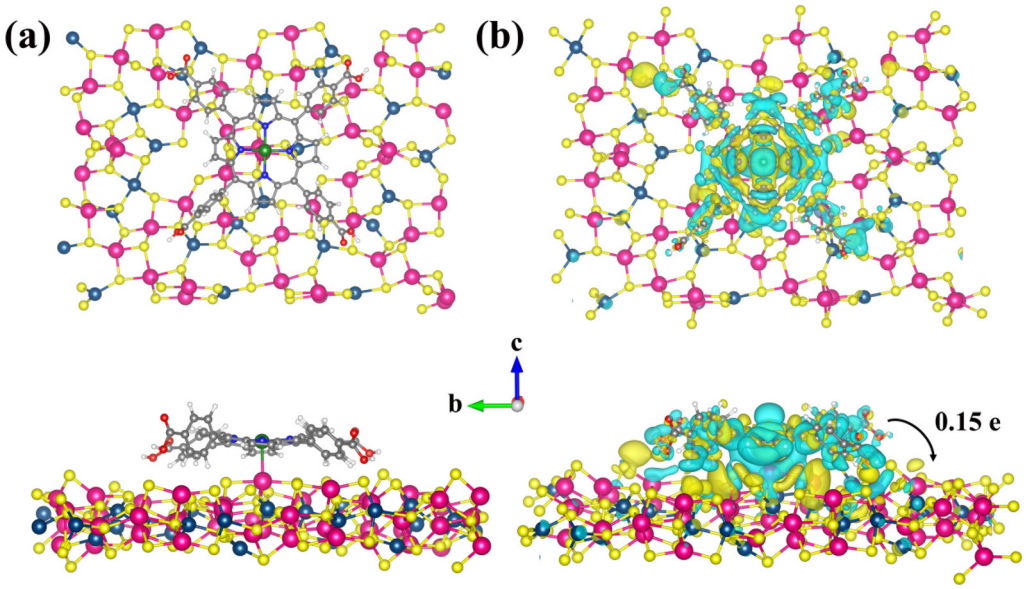

Fig. 8 (a) Top and side views of the Pd-PMOFs@$ZnIn_2S_4$ (102) heterostructure and (b) the corresponding charge density difference and the path of electron transfer.

were aggregated and depleted at the junctional interface between ZIS and the porphyrin ring centered on Pd atoms, respectively, demonstrating that electrons in Pd-PMOFs were transferred toward ZIS along the channel. Based on the analysis of the Bader charge change, the net charge of Pd from the primitive Pd-PMOFs was 0.741. After loading the ZIS nanosheets, the net charge of Pd in the Pd-PMOFs@ZIS composite increased to 0.777. As a result, electrons hopped from the Pd-PMOF carriers onto the ZIS crystal planes, and the number of transferred electrons was calculated to be 0.15 |e|, further verifying the intense interfacial effect in the Pd-PMOFs@ZIS heterojunction.[54]

From the above results, the proposed mechanism of the Pd-PMOFs@ZIS photocatalyst under visible light irradiation ($\lambda \geq$

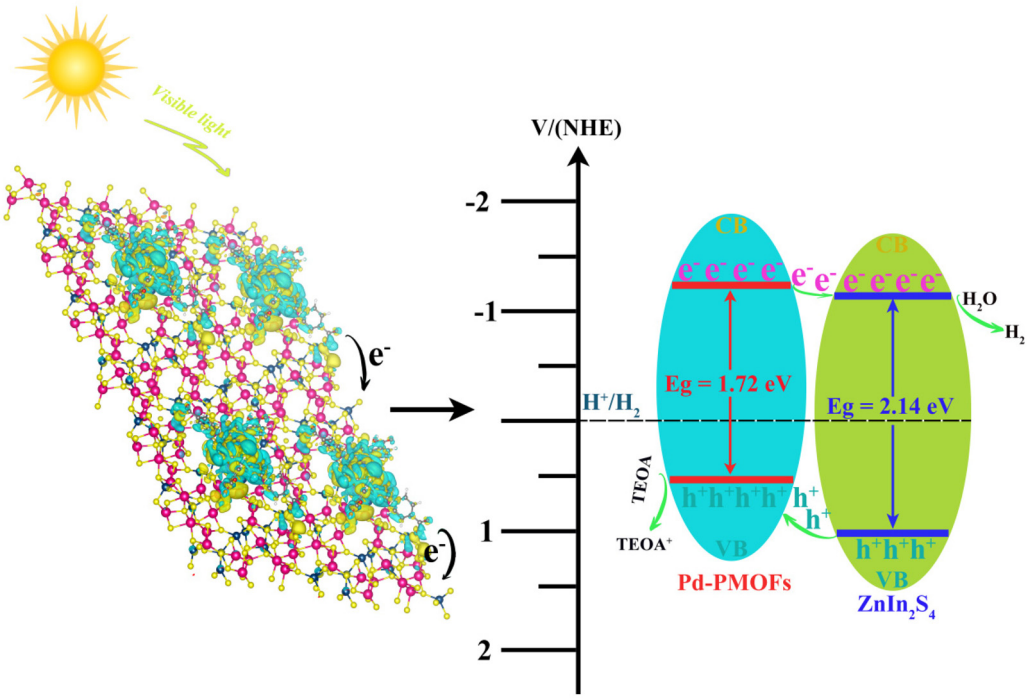

Fig. 9 Schematic illustration of charge transfer over the Pd-PMOFs@ZIS heterojunction for photocatalytic water splitting.

420 nm) is proposed for hydrogen production, as illustrated in Fig. 9. As mentioned previously, the Pd-PMOFs@ZIS heterojunction is a type II staggered n–n junction. When the Pd-PMOFs@ZIS photocatalyst is stimulated by visible light, the photogenerated abundant electron groups can be excited into the respective conduction band (CB) of Pd-PMOFs and ZIS, leaving photoinduced holes in their valence band (VB).[55] Since the CB potential of Pd-PMOFs is more negative than that of ZIS, the photoinduced electrons can quickly transfer from Pd-PMOFs to ZIS.[56] Simultaneously, the photogenerated holes from the VB of ZIS can migrate to that of the Pd-PMOFs. In the process of light reaction, the accumulated holes in Pd-PMOFs are quenched through reaction with the TEOA sacrificial agent, which sustainably inhibits the charge recombination, thereby increasing the number of photogenerated electrons.[57–59] In addition, Pd ions have good H^+ trapping capability. Therefore, the adsorbed H^+ can combine with these abundant electrons to generate hydrogen gas. It should be emphasized that the construction of the Pd-PMOFs@ZIS heterojunction provides intimate interfaces for electron transport along the binary core–shell dimensions and accelerates the charge disjunction, which has an energetic impact on the improvement of the hydrogen production performance of the photocatalysts.

4. Conclusions

In conclusion, the novel binary-shelled Pd-PMOFs@ZIS heterostructures were designed and constructed by the *in situ* growth of $ZnIn_2S_4$ nanosheets on Pd-PMOF carriers utilizing a simple hydrothermal method. The hierarchical binary structure for Pd-PMOFs@ZIS composites possessed extensive active sites, good visible light trapping ability and remarkable charge separation efficiency. Under visible light irradiation, the optimized Pd-PMOFs@ZIS photocatalyst displayed an obviously improved photocatalytic H_2 evolution activity of 8200.25 μmol h^{-1} g^{-1} with an apparent quantum efficiency of 13.17% at 420 nm, about 24.07 times higher than that of pure ZIS. Meanwhile, such a heterostructure presented extraordinary sustainability after consecutive cycles. Detailed characterization and DFT calculations indicated that the construction of binary-shelled heterostructures created electron migration channels, promoting the transfer of photogenerated electrons from Pd-PMOFs to the ZIS interface, which well suppressed the recombination of photoexcited electron–hole pairs. As a result, a significantly strengthened photocatalytic hydrogen production performance was acquired. The new-fashioned binary core–shell heterojunction proposed in this work would supply an important guidance for the production of photocatalysts with highly efficient charge transfer.

Author contributions

Sheng Wang: data analysis and writing – original draft and editing. Huiyi Feng: data analysis and editing. Sheng Wang and Huiyi Feng contributed equally to this work and should be considered as co-first authors. Chenglong Zheng and Shihao Li: methodology. Shilu Fan and Yi-Si Feng: conceptualization, resources, and funding acquisition.

Conflicts of interest

There are no conflicts to declare.

Acknowledgements

The work was supported by the National Natural Science Foundation of China (21971050).

References

1 D. D. La, H. H. Ngo, D. D. Nguyen, N. T. Tran, H. T. Vo, X. H. Nguyen, S. W. Chang, W. J. Chung and M. D. B. Nguyen, Advances and prospects of porphyrin-based nanomaterials via self-assembly for photocatalytic applications in environmental treatment, *Coord. Chem. Rev.*, 2022, **463**, 214543.
2 H. Yang, R. Shi, L. Shang and T. Zhang, Recent Advancements of Porphyrin-Like Single-Atom Catalysts: Synthesis and Applications, *Small Struct.*, 2021, **2**, 2100007.
3 V. Pascanu, G. González Miera, A. K. Inge and B. Martín-Matute, Metal–Organic Frameworks as Catalysts for Organic Synthesis: A Critical Perspective, *J. Am. Chem. Soc.*, 2019, **141**, 7223–7234.
4 Z. X. Cai, Z. L. Wang, J. Kim and Y. Yamauchi, Hollow Functional Materials Derived from Metal–Organic Frameworks: Synthetic Strategies, Conversion Mechanisms, and Electrochemical Applications, *Adv. Mater.*, 2019, **31**, 1804903.
5 S. Li, Z. Chen, L. Tan, Q. Wu, X. Ren, C. Fu, M. Niu, H. Li and X. Meng, MOF@COF nanocapsule for the enhanced microwave thermal-dynamic therapy and anti-angiogenesis of colorectal cancer, *Biomaterials*, 2022, **283**, 121472.
6 Y. Z. Chen, Z. U. Wang, H. Wang, J. Lu, S. H. Yu and H. L. Jiang, Singlet oxygen-engaged selective photo-oxidation over Pt nanocrystals/porphyrinic MOF: the roles of photothermal effect and Pt electronic state, *J. Am. Chem. Soc.*, 2017, **139**, 2035–2044.
7 X. Wu, X. Feng, J. Yuan, X. Yang, H. Shu, C. Yang, Z. Liu, J. Peng, E. Liu, S. Tan and P. Gao, Thiophene functionalized porphyrin complexes as novel bipolar organic cathodes with high energy density and long cycle life, *Energy Storage Mater.*, 2022, **46**, 252–258.
8 H. M. Castro-Cruz and N. A. Macías-Ruvalcaba, Porphyrin-catalyzed electrochemical hydrogen evolution reaction. Metal-centered and ligand-centered mechanisms, *Coord. Chem. Rev.*, 2022, **458**, 214430.
9 D. X. Zhang, H. Q. Yuan, H. Wang, A. Ali, W. H. Wen, A. N. Xie, S. Z. Zhan and H. Y. Liu, Transition metal tetra-

pentafluorophenyl porphyrin catalyzed hydrogen evolution from acetic acid and water, *Transition Met. Chem.*, 2017, **42**, 1–10.

10 J. Y. Zeng, M. K. Zhang, M. Y. Peng, D. Gong and X. Z. Zhang, Porphyrinic metal-organic frameworks coated gold nanorods as a versatile nanoplatform for combined photodynamic/photothermal/chemotherapy of tumor, *Adv. Funct. Mater.*, 2018, **28**, 1705451.

11 X. Liu, Z. Yan, Y. Zhang, Z. Liu, Y. Sun, J. Ren and X. Qu, Two-dimensional metal–organic framework/enzyme hybrid nanocatalyst as a benign and self-activated cascade reagent for in vivo wound healing, *ACS Nano*, 2019, **13**, 5222–5230.

12 P. Zhao, J. Wang, X. Han, J. Liu, Y. Zhang and B. Van der Bruggen, Zr-porphyrin metal–organic framework-based photocatalytic self cleaning membranes for efficient dye removal, *Ind. Eng. Chem. Res.*, 2021, **60**, 1850–1858.

13 L. Jin, S. Lv, Y. Miao, D. Liu and F. Song, Recent development of porous porphyrin-based nanomaterials for photocatalysis, *ChemCatChem*, 2021, **13**, 140–152.

14 M. Jafarzadeh, Recent progress in the development of MOF-based photocatalysts for the photoreduction of Cr(VI), *ACS Appl. Mater. Interfaces*, 2022, **14**, 24993–25024.

15 Q. Liu, H. Cong and H. Deng, Deciphering the spatial arrangement of metals and correlation to reactivity in multivariate metal–organic frameworks, *J. Am. Chem. Soc.*, 2016, **138**, 13822–13825.

16 W. Sheng, H. Hao, F. Huang, F. Zhang and X. Lang, 2D Ti-based metal–organic framework photocatalysis for red light-driven selective aerobic oxidation of sulfides, *Chem. Eng. J.*, 2022, **430**, 133071.

17 F. Leng, H. Liu, M. Ding, Q.-P. Lin and H.-L. Jiang, Boosting photocatalytic hydrogen production of porphyrinic MOFs: the metal location in metalloporphyrin matters, *ACS Catal.*, 2018, **8**, 4583–4590.

18 X. Wang, X. Zhang, W. Zhou, L. Liu, J. Ye and D. Wang, An ultrathin porphyrin-based metal–organic frameworks for efficient photocatalytic H_2 production under visible-light irradiation, *Nano Energy*, 2019, **62**, 250–258.

19 G. Lan, Y. Y. Zhu, S. S. Veroneau, Z. Xu, D. Micheroni and W. Lin, Electron injection from photoexcited metal-organic framework ligands to Ru_2 secondary building units for visible light-driven hydrogen evolution, *J. Am. Chem. Soc.*, 2018, **140**, 5326–5329.

20 W. Liu, Z. Guo, Z. Jin, D. Chen, T. Lu, P. Jia and H. Xing, Visible light-driven sonophotocatalysis for enhanced Cr(VI) reduction over mixed-linker zirconium-porphyrin MOFs, *Catal. Sci. Technol.*, 2022, **12**, 2176–2183.

21 Z. X. Sun, K. Sun, M.-L. Gao, Ö. Metin and H. L. Jiang, Optimizing Pt electronic states through formation of Schottky junction on non-reducible metal–organic frameworks for enhanced photocatalysis, *Angew. Chem., Int. Ed.*, 2022, **61**, e202206108.

22 S. Jayachitra, D. Mahendiran, P. Ravi, P. Murugan and M. Sathish, Highly conductive $NiSe_2$ nanoparticle as a co-catalyst over TiO_2 for enhanced photocatalytic hydrogen production, *Appl. Catal., B*, 2022, **307**, 121159.

23 K. Li and W. D. Zhang, Creating graphitic carbon nitride based donor-π–acceptor-π–donor structured catalysts for highly photocatalytic hydrogen Evolution, *Small*, 2018, **14**, 1703599.

24 S. P. Tripathy, S. Subudhi, A. Ray, P. Behera, A. Bhaumik and K. Parida, Mixed-valence bimetallic Ce/Zr MOF-based nanoarchitecture: a visible-light-active photocatalyst for ciprofloxacin degradation and hydrogen evolution, *Langmuir*, 2022, **38**, 1766–1780.

25 X. W. Li, S. W. Lu, J. Y. Yi, L. J. Shen, Z. H. Chen, H. Xue, Q. R. Qian and M. Q. Yang, Ultrathin two-dimensional $ZnIn_2S_4$/Nix-B heterostructure for high-performance photocatalytic fine chemical synthesis and H_2 generation, *ACS Appl. Mater. Interfaces*, 2022, **14**, 25297–25307.

26 J. Wang, S. J. Sun, R. Zhou, Y. Z. Li, Z. T. He, H. Ding, D. M. Chen and W. H. Ao, A review: synthesis, modification and photocatalytic applications of $ZnIn_2S_4$, *J. Mater. Sci. Technol.*, 2021, **78**, 1–19.

27 S. Q. Zhang, X. Liu, C. B. Liu, S. L. Luo, L. L. Wang, T. Cai, Y. X. Zeng, J. L. Yuan, W. Y. Dong, Y. Pei and Y. T. Liu, MoS_2 quantum dots growth induced by S vacancy in $ZnIn_2S_4$ monolayer: atomic-level heterostructure for photocatalytic hydrogen production, *ACS Nano*, 2018, **12**, 751–758.

28 S. B. Wang, B. Y. Guan and X. W. David Lou, Construction of $ZnIn_2S_4$-In_2O_3 hierarchical tubular heterostructures for efficient CO_2 photoreduction, *J. Am. Chem. Soc.*, 2018, **140**, 5037–5040.

29 P. X. Jin, L. Wang, X. L. Ma, R. Lian, J. W. Huang, H. D. She, M. Y. Zhang and Q. Z. Wang, Construction of hierarchical $ZnIn_2S_4$@PCN-224 heterojunction for boosting photocatalytic performance in hydrogen production and degradation of tetracycline hydrochloride, *Appl. Catal., B*, 2021, **284**, 119762.

30 H. Liu, J. Zhang and D. Ao, Construction of heterostructured $ZnIn_2S_4$@NH_2-MIL-125(Ti) nanocomposites for visible-light-driven H_2 production, *Appl. Catal., B*, 2018, **221**, 433–442.

31 B. Lin, H. Li, H. An, W. B. Hao, J. J. Wei, Y. Z. Dai, C. S. Ma and G. D. Yang, Preparation of 2D/2D g-C_3N_4 nanosheet@$ZnIn_2S_4$ nanoleaf heterojunctions with well-designed high-speed charge transfer nanochannels towards high-efficiency photocatalytic hydrogen evolution, *Appl. Catal., B*, 2018, **220**, 542–552.

32 R. R. Yuan, J. L. Qiu, C. L. Yue, C. Shen, D. W. Li, C. Q. Zhu, F. Q. Liu and A. M. Li, Self-assembled hierarchical and bifunctional MIL-88A(Fe)@$ZnIn_2S_4$ heterostructure as a reusable sunlight-driven photocatalyst for highly efficient water purification, *Chem. Eng. J.*, 2020, **401**, 126020.

33 S. Wang, Y. X. Qi, C. L. Zheng, S. L. Fan and Y. S. Feng, Facile synthesis of porous 3D honeycomb-like $ZnIn_2S_4$ microspheres with improved photocatalytic activity for hydrogen evolution, *New J. Chem.*, 2022, **46**, 20866–20873.

34 R. Q. Jiang, L. Mao, Y. L. Zhao, J. Y. Zhang, E. B. Chubenko, V. Bondarenko, Y. W. Sui, X. Q. Gu and X. Y. Cai, 1D/2D

$CeO_2/ZnIn_2S_4$ Z-scheme heterojunction photocatalysts for efficient H_2 evolution under visible light, *Sci. China Mater.*, 2023, **66**, 139–149.

35 S. Wang, S. H. Li, H. Y. Feng, W. Q. Yang and Y. S. Feng, Visible-light-driven porphyrin-based bimetallic metal–organic frameworks for selective photoreduction of nitro compounds under mild conditions, *ACS Appl. Mater. Interfaces*, 2023, **15**, 4845–4856.

36 Q. Zhang, H. J. Gu, X. H. Wang, L. F. Li, J. H. Zhang, H. H. Zhang, Y. F. Li and W. L. Dai, Robust hollow tubular $ZnIn_2S_4$ modified with embedded metal-organic-framework-layers: extraordinarily high photocatalytic hydrogen evolution activity under simulated and real sunlight irradiation, *Appl. Catal., B*, 2021, **298**, 120632.

37 G. C. Zuo, S. S. Ma, Z. Z. Yin, W. Y. Chen, Y. T. Wang, Q. Y. Ji, Q. M. Xian, S. G. Yang and H. He, Z-scheme modulated charge transfer on $InVO_4$@$ZnIn_2S_4$ for durable overall water splitting, *Small*, 2023, 2207031.

38 X. Shi, C. Dai, X. Wang, J. Hu, J. Zhang, L. Zheng, L. Mao, H. Zheng and M. Zhu, Protruding Pt single-sites on hexagonal $ZnIn_2S_4$ to accelerate photocatalytic hydrogen evolution, *Nat. Commun.*, 2022, **13**, 1287.

39 Z. X. Zeng, Y. Su, X. Quan, W. Y. Choi, G. H. Zhang, N. Liu, B. Kim, S. Chen, H. T. Yu and S. S. Zhang, Single-atom platinum confined by the interlayer nanospace of carbon nitride for efficient photocatalytic hydrogen evolution, *Nano Energy*, 2020, **69**, 104409.

40 Y. Pan, X. Z. Yuan, L. B. Jiang, H. B. Y. J. Zhang, H. Wang, R. P. Guan and G. M. Zeng, Recent advances in synthesis, modification and photocatalytic applications of micro/nano-structured zinc indium sulfide, *Chem. Eng. J.*, 2018, **354**, 407–431.

41 A. Hu, W. Q. Lv, T. Y. Lei, W. Chen, Y. Hu, C. Z. Shu, X. F. Wang, L. X. Xue, J. W. Huang, X. C. Du, H. B. Wang, K. Tang, C. H. Gong, J. Zhu, W. D. He, J. P. Long and J. Xiong, Heterostructured $NiS_2/ZnIn_2S_4$ realizing toroid-like Li_2O_2 deposition in lithium–oxygen batteries with low-donor-number solvents, *ACS Nano*, 2020, **14**, 3490–3499.

42 O. Cavdar, M. Baluk, A. Malankowska, A. Żak, W. Lisowski, T. Klimczuk and A. Zaleska-Medynska, Photocatalytic hydrogen evolution from glycerol-water mixture under visible light over zinc indium sulfide ($ZnIn_2S_4$) nanosheets grown on bismuth oxychloride (BiOCl) microplates, *J. Colloid Interface Sci.*, 2023, **640**, 578–587.

43 T. Zhu, X. Ye, Q. Zhang, Z. Hui, X. Wang and S. Chen, Efficient utilization of photogenerated electrons and holes for photocatalytic redox reactions using visible light-driven Au/$ZnIn_2S_4$ hybrid, *J. Hazard. Mater.*, 2019, **367**, 277–285.

44 C. Q. Li, X. Du, S. Jiang, Y. Liu, Z. L. Niu, Z. Y. Liu, S. S. Yi and X. Z. Yue, Constructing direct Z-scheme heterostructure by enwrapping $ZnIn_2S_4$ on CdS hollow cube for efficient photocatalytic H_2 generation, *Adv. Sci.*, 2022, **9**, 2201773.

45 L. Wang, J. Guo, G. Yang, D. Yu, D. Wang, F. Guo and W. Guan, Rational tailoring of the electronic structure for the Sr*x*NaTa*y*O_3 semiconductor: insights into its enhanced photoactivity and optical property, *Chemosphere*, 2021, **273**, 129748.

46 H. Che, C. Liu, G. Che, G. Liao, H. Dong, C. Li, N. Song and C. Li, Facile construction of porous intramolecular g-C_3N_4-based donor-acceptor conjugated copolymers as highly efficient photocatalysts for superior H_2 evolution, *Nano Energy*, 2020, **67**, 104273.

47 C. Liu, Q. F. Zhang and Z. G. Zou, Recent advances in designing $ZnIn_2S_4$-based heterostructured photocatalysts for hydrogen evolution, *J. Mater. Sci. Technol.*, 2023, **139**, 167–188.

48 T. M. Su, Q. Shao, Z. Z. Qin, Z. H. Guo and Z. L. Wu, Role of interfaces in two-dimensional photocatalyst for water splitting, *ACS Catal.*, 2018, **8**, 2253–2276.

49 Y. Q. Zhong, R. Wang, J. H. Chen, C. Duan, Z. Y. Huang, S. Yu, H. Guo and Y. Zhou, Surface-terminated hydroxyl groups for deciphering the facet-dependent photocatalysis of anatase TiO_2, *ACS Appl. Mater. Interfaces*, 2022, **14**, 17601–17609.

50 J. C. Jiao, H. C. Si, J. B. Xu, T. Zhang and Q. X. Han, Photocatalytic multielectron reduction of nitroarenes to anilines by utilizing an electron-storable polyoxometalate-based metal–organic framework, *ACS Appl. Mater. Interfaces*, 2022, **14**, 16386–16393.

51 X. Q. Huang, S. Liu, Z. Zhou, H. Z. Zhang, Z. Y. Gao, G. D. Shen, H. W. Wang, Z. Wang, Q. X. Yao and D. Sun, The tail of imidazole regulated the assembly of two robust sandwich-type polyoxotungstate-based open frameworks with efficient visible-white-light-driven catalytic oxidation of sulfides, *Inorg. Chem. Front.*, 2023, **10**, 1465–1474.

52 X. L. Zheng, Y. M. Song, Y. H. Liu, Y. Q. Yang, D. X. Wu, Y. J. Yang, S. Y. Feng, J. Li, W. F. Liu, Y. J. Shen and X. L. Tian, $ZnIn_2S_4$-based photocatalysts for photocatalytic hydrogen evolution via water splitting, *Coord. Chem. Rev.*, 2023, **475**, 214898.

53 X. H. Wang, X. H. Wang, T. Y. Shi, A. Meng, T. Q. Yang, M. M. Zhang, L. Wang, G. C. Li, J. F. Huang, X. Yu and Z. J. Li, "O-S" charge transfer mechanism guiding design of a $ZnIn_2S_4$/$SnSe_2/In_2Se_3$ heterostructure photocatalyst for efficient hydrogen production, *ACS Catal.*, 2023, **13**, 1020–1032.

54 P. Basyach, P. K. Prajapati, S. S. Rohman, K. Sonowal, L. Kalita, A. Malik, A. K. Guha, S. L. Jain and L. Saikia, Visible light-active ternary heterojunction photocatalyst for efficient CO_2 reduction with simultaneous amine oxidation and sustainable H_2O_2 production, *ACS Appl. Mater. Interfaces*, 2023, **15**, 914–931.

55 J. D. Hu, C. Chen, Y. Zheng, G. P. Zhang, C. X. Guo and C. M. Li, Spatially separating redox centers on Z-scheme $ZnIn_2S_4/BiVO_4$ Hierarchical heterostructure for highly efficient photocatalytic hydrogen evolution, *Small*, 2020, **16**, 2002988.

56 S. Zhao, Q. Liang, W. Gao, M. Zhou, C. Yao, S. Xu and Z. Y. Li, In situ growth of $ZnIn_2S_4$ on MOF-derived Ni–Fe LDH to construct ternary-shelled nanotubes for efficient photocatalytic hydrogen evolution, *Inorg. Chem.*, 2021, **60**, 9762–9772.

57 Z. Z. Li, H. Z. Li, S. J. Wang, F. Yang and W. Zhou, Mesoporous black $TiO_2/MoS_2/Cu_2S$ hierarchical tandem heterojunctions toward optimized photothermal-photocatalytic fuel production, *Chem. Eng. J.*, 2022, **427**, 131830.
58 B. J. Sun, W. Zhou, H. Z. Li, L. P. Ren, P. Z. Qiao, W. Li and H. G. Fu, Synthesis of particulate hierarchical tandem heterojunctions toward optimized photocatalytic hydrogen production, *Adv. Mater.*, 2018, **30**, 1804282.
59 Y. C. Wang, M. J. Liu, C. X. Wu, J. P. Gao, M. Li, Z. P. Xing, Z. Z. Li and W. Zhou, Hollow nanoboxes $Cu_{2-x}S@ZnIn_2S_4$ core-Shell S-scheme heterojunction with broad-spectrum response and enhanced photothermal-photocatalytic performance, *Small*, 2022, **18**, 2202544.